

PUBLISHED VERSION

Weijie Gao, Xiongbin Yu, Masayuki Fujita, Tadao Nagatsuma, Christophe Fumeaux and Withawat Withayachumnankul

Effective-medium-cladded dielectric waveguides for terahertz waves

Optics Express, 2019; 27(26):38721-38734

DOI: <http://dx.doi.org/10.1364/OE.382181>

© 2019 Optical Society of America under the terms of the OSA Open Access Publishing Agreement

PERMISSIONS

https://www.osapublishing.org/submit/review/copyright_permissions.cfm

Open Access Publishing Agreement




OSA's "Copyright Transfer and Open Access Publishing Agreement" (OAPA) is the default option for most authors when publishing in one of our fully open access journals or when opting for open access in our hybrid journals. All articles published under our OAPA are freely accessible, while copyright is transferred to OSA. Authors may post the published version of their article to their personal website, institutional repository, or a repository required by their funding agency. Authors and readers may use, reuse, and build upon the article, or use it for text or data mining, as long as the purpose is non-commercial and appropriate attribution is maintained.

6 July 2020

<http://hdl.handle.net/2440/124056>



Effective-medium-cladded dielectric waveguides for terahertz waves

WEIJIE GAO,¹  XIONGBIN YU,²  MASAYUKI FUJITA,² TADAO NAGATSUMA,²  CHRISTOPHE FUMEUX,¹ AND WITHAWAT WITHAYACHUMNANKUL^{1,*}

¹*Terahertz Engineering Laboratory, School of Electrical and Electronic Engineering, The University of Adelaide, South Australia 5005, Australia*

²*Graduate School of Engineering Science, Osaka University, 1-3 Machikaneyama, Toyonaka, Osaka 560-8531, Japan*

*withawat@adelaide.edu.au

Abstract: Terahertz integrated platforms with high efficiency are crucial in a broad range of applications including terahertz communications, radar, imaging and sensing. One key enabling technology is wideband interconnection. This work proposes substrate-less all-dielectric waveguides defined by an effective medium with a subwavelength hole array. These self-supporting structures are built solely into a single silicon wafer to minimize significant absorption in metals and dielectrics at terahertz frequencies. In a stark contrast to photonic crystal waveguides, the guiding mechanism is not based on a photonic bandgap but total internal reflections. The waveguides are discussed in the context of terahertz communications that imposes stringent demands on performance. Experimental results show that the realized waveguides can cover the entire 260–400 GHz with single dominant modes in both orthogonal polarizations and an average measured attenuation around 0.05 dB/cm. Limited by the measurement setup, the maximum error-free data rate up to 30 Gbit/s is experimentally achieved at 335 GHz on a 3-cm waveguide. We further demonstrate the transmission of uncompressed 4K-resolution video across this waveguide. This waveguide platform promises integration of diverse active and passive components. Thus, we can foresee it as a potential candidate for the future terahertz integrated circuits, in analogy to photonic integrated circuits at optical frequencies. The proposed concept can potentially benefit integrated optics at large.

© 2019 Optical Society of America under the terms of the [OSA Open Access Publishing Agreement](#)

1. Introduction

Data traffic has grown exponentially with a dramatically increasing proportion of the world population accessing online services [1]. This trend has been exacerbated by the rapid growth in usage of high-quality multimedia content with huge data volume. Therefore, higher channel capacities in wireless transmission are in demand to support not only mobile links but also links among static nodes in the backbones. However, an increased data throughput would pressure the already congested microwave and millimetre-wave channels [2]. According to the Shannon-Hartley theorem, the channel capacity can be improved by increasing the bandwidth of the carrier, subject to signal quality [3].

Bridging electronics and optics, the terahertz spectrum that spans the frequency range from 0.1 to 10 THz is an ideal candidate to support high-speed wireless line-of-sight transmission [2,4], owing to its ultra-wide absolute bandwidth. In theory, the prospective data rate carried by a terahertz channel can reach 1 Tbit/s over the distance of several kilometres [5]. However, reaching this theoretical capacity calls for solutions to several challenges [6], including the significant power losses in integrated transmitter and receiver components that compromise signal quality. This issue can be mitigated by using bulky discrete components with trade-offs in dispersion, fabrication complexity, and compactness [7,8]. Hence, to realize integrated terahertz

communications systems with enhanced performance, planar interconnects with low loss and low dispersion in broadband are vital [9–17].

At terahertz frequencies, conventional planar metallic transmission lines, such as microstrip lines and coplanar waveguides, impose significant transmission losses in the order of several dB/cm [18–20]. This is caused by their strong field confinement, together with substantial ohmic and dielectric losses at high frequencies. The same issues apply to the substrate integrated waveguides that have been widely used in millimetre-wave applications [21]. An alternative is substrate-integrated image guide (SIIG) technology that employs metal-grounded dielectric waveguides [11,12]. This type of waveguide could achieve an average transmission loss of 0.45 dB/cm from 85 to 90 GHz [11], and 0.35 dB/cm from 110 to 170 GHz [12]. While these metal-based guiding structures are reasonably efficient at microwave and millimetre-wave frequencies, they are not suitable to terahertz integrated systems due to increasing metal and dielectric losses.

Inspired by guided-wave optics [22,23], all-dielectric waveguides with low transmission losses have been investigated at terahertz frequencies in the past. For example, dielectric waveguides were proposed with an average propagation loss of 0.087 dB/cm over two bands (90–140 GHz and 140–220 GHz) [24]. In spite of their low losses and low dispersion, such bare dielectric waveguides have limitations in realizing integrated systems since they lack self-support and support for other components. To improve the integrability, silicon-on-insulator (SOI) waveguides were proposed [13,14], where the average loss was 0.46 dB/cm over 500 to 580 GHz [13]. With structural resemblance, a dielectric microstrip line concentrates the energy in the low-index oxide spacer [14]. In this case, the loss varied from 0.23 to 1.2 dB/cm over 750 to 925 GHz [14]. However, the losses imposed by additional supporting materials are not negligible [25]. To achieve an integrated waveguide platform with low loss and structural simplicity, all-dielectric 2D photonic crystal waveguides built from a single silicon wafer were proposed [15,17]. Silicon, as the only constituent material, has extremely low dissipation. As such, a propagation loss of less than 0.1 dB/cm could be demonstrated from 319 to 337 GHz [15], while another similar design could yield an enhanced bandwidth of 324–361 GHz with comparable losses [17]. However, these photonic crystal waveguides have relatively narrow bandwidths and strong in-band dispersion related to the intrinsic photonic bandgap (PBG) phenomenon.

In this paper, we propose a class of self-supporting all-dielectric waveguides. The proposed substrate-less waveguides are constructed solely from a high-resistivity silicon wafer that has exceptionally low loss and low dispersion at terahertz frequencies [26]. A silicon waveguide core is surrounded by in-plane effective-medium claddings, which are realized by periodic perforation of the silicon slab. This pure-silicon platform allows integration of active and passive components, as demonstrated in photonic crystal waveguides [27,28]. In a stark contrast to photonic crystal waveguides, the perforation period of the proposed waveguide is in the deep subwavelength region. In this way, the perforated medium behaves like a homogeneous material rather than a bandgap material [29]. Compared with a bandgap material, this chosen cladding results in a great bandwidth enhancement with low dispersion in both orthogonal modes—the properties much needed in diverse terahertz applications, but not available from photonic crystal waveguides. Compared to the SIIG waveguides, the proposed design is free from metal thus achieving lower transmission losses, while being able to sustain two orthogonal dominant modes. Compared to the SOI waveguides, the proposed design is self-supporting and does not require additional materials that would contribute to propagation losses. In Section II, the waveguide design and the modal analysis will be presented. Section III will discuss the waveguide fabrication and measurements, where the transmission and high-speed terahertz communications over this waveguide will be demonstrated.

2. Waveguide design and analysis

2.1. Overview

As shown in Figs. 1(a)–1(c), the proposed integrated all-dielectric waveguide comprises a waveguide solid core and in-plane effective medium claddings, both built monolithically into a silicon slab. The unperforated areas are for handling purposes and do not interfere with the propagation modes of the waveguide. The silicon slab with a thickness of $200\ \mu\text{m}$ has a relative permittivity ϵ_{Si} of 11.68 (an equivalent refractive index n_{Si} of 3.418) and a resistivity of $20\ \text{k}\Omega\text{-cm}$. Such high-resistivity silicon is nondispersive and offers extremely low loss, with power absorption coefficients less than $0.01/\text{cm}$ in the entire terahertz band [26]. The effective medium is realized by periodically perforating the silicon slab with cylindrical air holes in a hexagonal lattice, with a period a much smaller than the shortest guided wavelength λ_g as shown in Fig. 1(d). The effective relative permittivity of the effective medium falls between those of air and silicon, and is determined by the perforation period a and the hole diameter d . Owing to the refractive index contrast between the core and the claddings, i.e., between silicon and effective medium in plane, and silicon and air out of plane, the waves can be confined within the waveguide core by total internal reflections. Due to the low-index claddings in both transverse dimensions, the waveguide supports two orthogonal fundamental modes E_{11}^x and E_{11}^y , namely with the polarization for the E_{11}^x mode being parallel to the slab, while being perpendicular to the slab for the E_{11}^y mode. Given properly designed waveguide width, perforation period, and hole diameter, the waveguide can operate with a single mode over 260 to 400 GHz (WR-2.8 band) for each polarization.

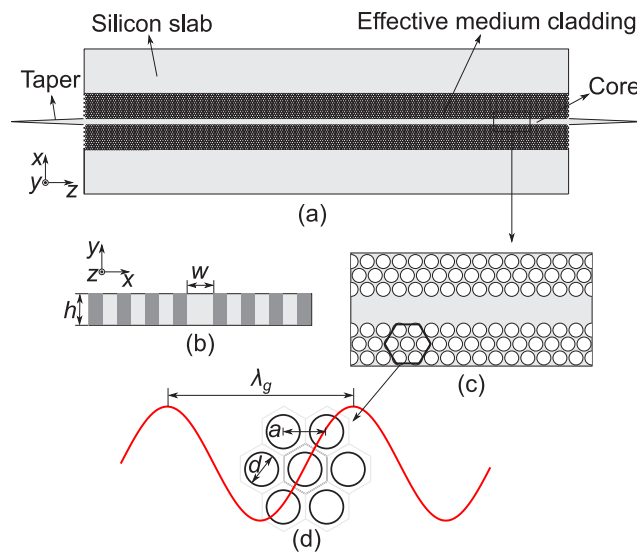


Fig. 1. Effective-medium-cladded dielectric waveguide. (a) Top view, (b) magnified cross-sectional view, (c) magnified view of waveguide core and claddings, and (d) hexagonal lattice of the effective medium cladding with perforation period a and hole diameter d . The period a is a quarter of the shortest guided wavelength λ_g . This effective-medium cladding is completely different from a photonic crystal cladding that requires a periodicity close to half a guided wavelength. As a result, the waveguide can be classified as a dielectric waveguide, not a photonic crystal waveguide. The tapers are coupling structures to be inserted into the hollow metallic waveguides required for simulations and measurements. The dimensions of the final design are: $h = 200\ \mu\text{m}$, $w = 160\ \mu\text{m}$, $a = 100\ \mu\text{m}$, $d = 90\ \mu\text{m}$. It is noted that the lateral unperforated silicon regions are for handling purpose, and they do not interfere with the guided modes.

Despite their similar appearances, the proposed effective-medium-cladded dielectric waveguides are fundamentally different from the photonic crystal waveguides [15,17] in terms of operation mechanism [29,30]. Specifically, the guidance of the photonic crystal waveguides relies on the bandgap effects. The bandgap material prohibits propagation modes by means of interference and thus confines the waves within the core. The realization of the bandgap materials is based on a variation in refractive indices of two alternating dielectric materials with the period equal to or longer than half of the guided wavelength to cause destructive interference. This guiding mechanism greatly limits the operation bandwidth, including strong in-band dispersion, and restricting the waveguide to one dominant mode. In contrast, the effective-medium-cladded waveguides rely merely on the total internal reflection attributed to the refractive index contrast between the waveguide core and the claddings. In this case, the purpose of the deeply sub-wavelength perforation is to lower the effective refractive index of the silicon slab to create an effective medium [29,31]. As such, we can expect a vastly extended bandwidth with low dispersion for orthogonal dominant modes. The considerations for the effective medium and waveguide modal analysis will be discussed in the following.

2.2. Effective medium

As shown in Fig. 1(d), the effective medium claddings are in the form of a hexagonal array of cylindrical thru-holes perforated into the silicon. The relative permittivity of the effective medium can be obtained by Maxwell–Garnett approximations [31,32], which are polarization-dependent. These approximations are valid only when the periodicity is subwavelength, where wave diffraction and scattering are negligible. In this way, the effective medium can be treated as a homogeneous material with an equivalent anisotropic permittivity tensor with respect to the macroscopic electromagnetic field [29,31]. Specifically, the relative permittivities for the E -field perpendicular and parallel to the axis of the cylindrical air hole are defined as ϵ_x and ϵ_y respectively. They are given as [32]

$$\epsilon_x = \epsilon_{\text{Si}} \frac{(\epsilon_0 + \epsilon_{\text{Si}}) + (\epsilon_0 - \epsilon_{\text{Si}})\zeta}{(\epsilon_0 + \epsilon_{\text{Si}}) - (\epsilon_0 - \epsilon_{\text{Si}})\zeta}, \quad (1)$$

$$\epsilon_y = \epsilon_{\text{Si}} + (\epsilon_0 - \epsilon_{\text{Si}})\zeta. \quad (2)$$

where ϵ_0 and ϵ_{Si} are the relative permittivities of the air and silicon respectively, while ζ represents the fill factor of the air volume in silicon. For a hexagonal lattice, the fill factor can be calculated from $(\pi d^2)/(2\sqrt{3}a^2)$, where d is the diameter of the cylindrical air hole and a is the period of the lattice. According to Eqs. (1)–(2), the effective relative permittivities for both polarizations are monotonously decreasing with the fill factor and varying between the values of silicon and air.

In addition to the subwavelength periodicity, the design process for the effective-medium claddings needs to account for the following considerations: (i) single mode operation, (ii) wave confinement and (iii) structural integrity. Since the cutoff frequencies of the higher-order modes are affected by the claddings, the effective relative permittivity must be selected properly to enable a single-mode operation for each polarization over the desired band. Specifically, a lower relative permittivity of the claddings would generate a lower propagation constant thus pushing the cutoff frequencies of higher-order modes upward. To obtain a well guided wave with its power mostly concentrated within the core, a higher refractive index contrast between the core and the claddings is preferred [33,34]. These two conditions can be satisfied with an effective medium having a larger portion of air. As a trade-off, a larger air portion in the claddings compromises mechanical strength of the platform.

By considering all those factors mentioned above, the periodicity a is selected as $100 \mu\text{m}$ in this design, corresponding to about $0.46\lambda_{\text{Si}}$, where λ_{Si} is the wavelength in bulk silicon at 400 GHz. This estimation is the worst case, since the guided wavelength is always larger than that in the bulk material. The hole diameter is chosen as $90 \mu\text{m}$ generating ϵ_x and ϵ_y of 2.75

and 3.84 respectively. These effective permittivities are much lower compared with the relative permittivity of bulk silicon of 11.68. In this work, a hexagonal lattice is adopted for mechanical strength of the platform. It is noted that given a subwavelength period between adjacent holes, the effective medium claddings could be defined in any lattice, e.g., hexagonal or square lattice to match the profile of the waveguide core.

2.3. Modal analysis

Marcatili's theory [33] is applied here to investigate the dispersion characteristics of the waveguide. According to this theory [33], the propagation constant β_z is a function of the operation wavelength λ , the width w and the height h of the waveguide core, as well as the relative permittivities of the

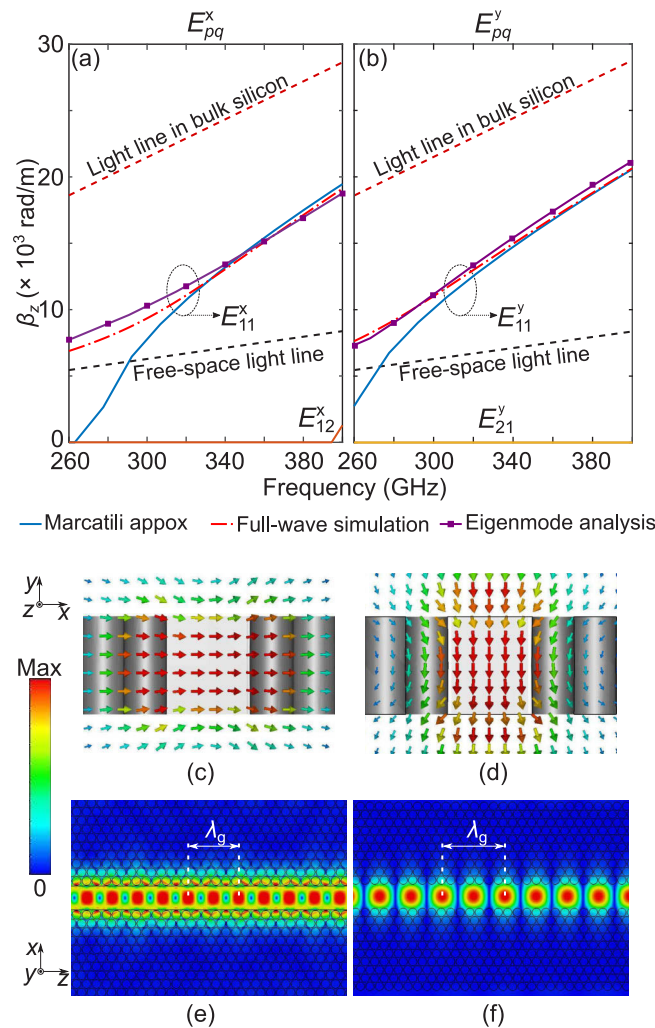


Fig. 2. Characteristics of the waveguide. Dispersion characteristics for (a) E_{pq}^x and (b) E_{pq}^y modes. Simulated E -field distributions in linear scale at 330 GHz for (c, e) E_{11}^x and (d, f) E_{11}^y modes in the cross-sectional and top views, respectively. The propagation constants in the case of full-wave simulation and Eigenmode analysis are obtained from CST Microwave Studio. The propagation constants for higher-order modes are obtained from Marcatili approximation, and these modes remain below the cutoff in this frequency range.

core and effective medium claddings. In the specific design presented in this paper, the height of the waveguide core is $200\ \mu\text{m}$, while its width is selected as $160\ \mu\text{m}$. Given the effective relative permittivity tensor of the claddings, the dispersion characteristics can be theoretically obtained. It is noted that Marcatili's theory has limitations in accurately predicting the dispersion behaviour of the fundamental modes at low frequencies owing to the mode approximations [33]. Therefore, Eigenmode analysis and full-wave simulations are performed in CST Microwave Studios to complement the analytical results.

As shown in Fig. 2(a)–2(b), the results from the three approaches for the fundamental modes are in good agreement, and converge at high frequencies. Within the operation frequency range from 260 to 400 GHz, the waveguide can work with low dispersion in single dominant modes for both polarizations. In addition, we can infer that the waves are tightly confined, as all the propagation constants for the E_{11}^x and E_{11}^y modes are well above the free-space light line. In addition, the higher-order mode appearing above 395 GHz for the horizontal polarization will not

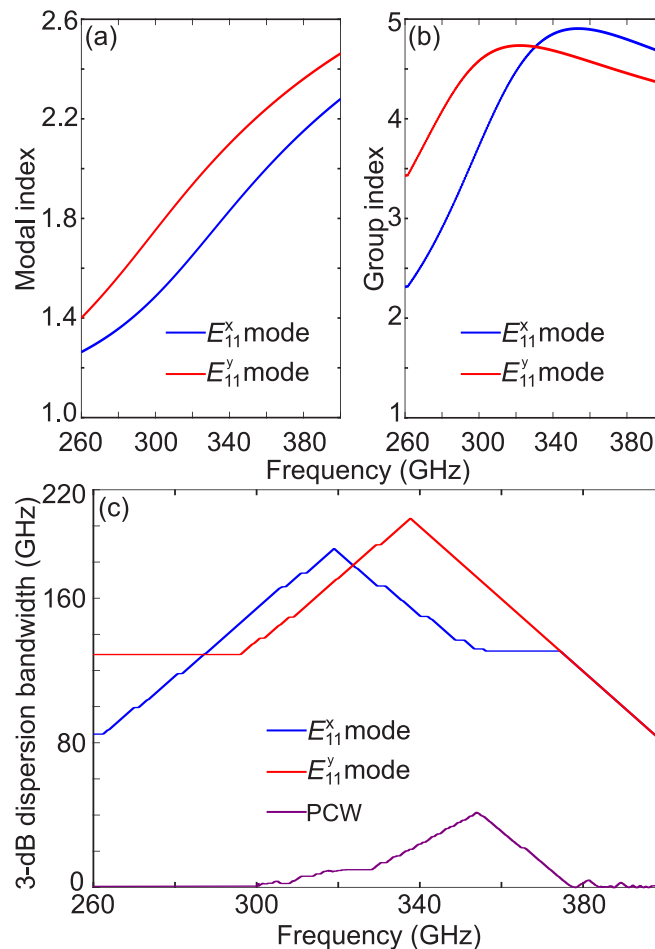


Fig. 3. Simulated dispersion characteristics. (a) Modal indices, (b) group indices, and (c) calculated 3-dB dispersion bandwidth for the effective-medium-cladded waveguide and photonic crystal waveguide. The lengths of the effective-medium-cladded waveguide and the bandwidth-enhanced photonic crystal waveguide [17] for 3-dB bandwidth calculation are 3 cm.

interfere with the dominant modes, since they have propagation constants below the light line, i.e., the wave confinement is extremely weak. However, the higher-order mode might cause slight radiation loss and reduce the waveguide efficiency. In this way, the bandwidth of the waveguide might need to be reduced to 260–395 GHz in some particular scenarios. The simulated E -field distributions for both dominant modes at 330 GHz, i.e., at the centre frequency, are shown in Figs. 2(c)–2(f).

It is observed that most of the power is concentrated within the waveguide core with evanescent fields extending a few rows into the claddings as shown in Figs. 2(e)–2(f). Based on the dispersion characteristics, the effective modal indices for the two dominant modes can be obtained. As shown in Fig. 3(a), the effective modal index for the E_{11}^x mode is lower than that for the E_{11}^y mode. This disparity results from the differences between the width and height of the waveguide core and between the in-plane and out-of-plane claddings [35]. Based on these modal indices, the periodicity of the effective medium amounts to only $0.3\lambda_g$, where λ_g is the shortest guided wavelength at 400 GHz. Derived from the modal indices, the group index for the E_{11}^x mode is found to be higher than that for the E_{11}^y over 260–335 GHz, while the trend inverses over 335–400 GHz as shown in Fig. 3(b).

The calculated 3-dB dispersion bandwidths based on the group delay [36] of a 3-cm waveguide for both the E_{11}^x and E_{11}^y modes are shown in Fig. 3(c). Owing to the low dispersion, the 3-dB bandwidth for each carrier frequency is high, i.e., the waveguide can support high-speed communications with ultra-broad bandwidth. The 3-dB dispersion bandwidth ranges from 80 to 185 GHz for the E_{11}^x mode, while it varies from 80 to 190 GHz for the E_{11}^y mode over the entire frequency range. The discrepancies of the bandwidth for the two modes are due to a slight difference in the dispersion characteristics. Compared to the bandwidth-enhanced photonic crystal waveguide (PCW) [17], the calculated 3-dB dispersion bandwidths of the proposed waveguide are much higher. This performance improvement is attributed to its extremely low in-band dispersion.

3. Experiments

To validate the design, waveguide samples with lengths of 1, 2 and 3 cm have been fabricated. The samples are obtained from a 4-inch intrinsic float-zone silicon wafer with a thickness of 200 μm and a resistivity of 20 $\text{k}\Omega\text{-cm}$. The fabrication is based on a standard deep reactive ion-etching (DRIE) process. The waveguide core with height of 200 μm and width of 160 μm is surrounded by the effective medium claddings that are made of cylindrical air holes in a hexagonal lattice with period of 100 μm and hole diameter of 90 μm . As mentioned earlier, the solid outer claddings are for handling purposes and do not interfere with the guided waves. To test the mechanical strength of the samples, the cladding on each side contains 24 rows of holes as shown in Fig. 4. The fabricated samples with various lengths show good mechanical strength. However, such a row number is excessive, because the cladding size must be designed with the considerations of wave confinement, structural compactness and mechanical strength. As shown in Figs. 2(e)–2(f), a minimal number of rows of around three is sufficient to accommodate the evanescent fields. It is noted that in the measurement the impact of the feeding waveguide on coupling cannot be neglected, and in this case, seven rows of holes for the cladding are preferred.

3.1. Transmission measurements

As shown in Figs. 5(a)–5(b), the transmission measurements are carried out using a terahertz electronic system. The continuous wave electronic source is constructed from a millimetre-wave signal generator and a nine-fold frequency multiplier. On the receiver side, a frequency mixer downconverts the terahertz signal to the intermediate frequency (IF) at 404.4 MHz by mixing with a local oscillator (LO) signal generated from the spectrum analyser. This setup works in the frequency range from 260 to 390 GHz. The system is equipped with WR-3 hollow metallic

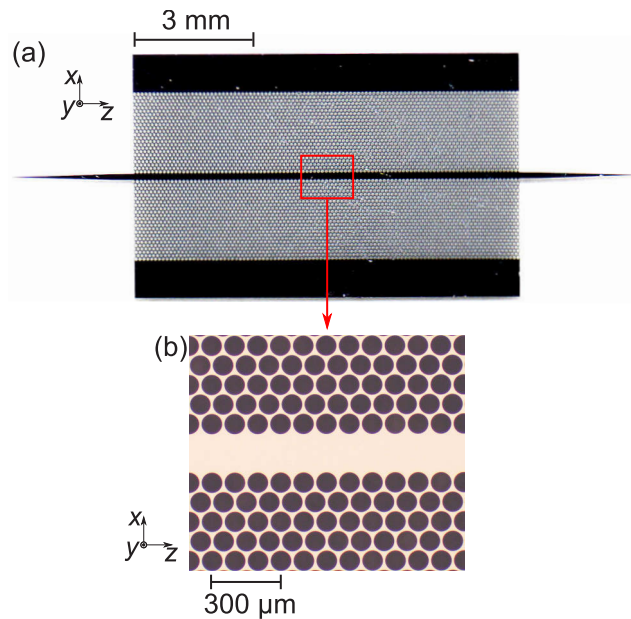
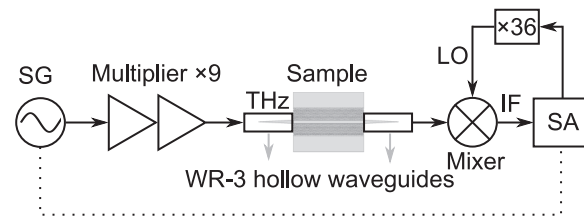


Fig. 4. Fabricated effective-medium-cladded dielectric waveguide. (a) 1 cm waveguide sample, and (b) magnified view of the effective-medium claddings. The design parameters are given in the caption of Fig. 1.

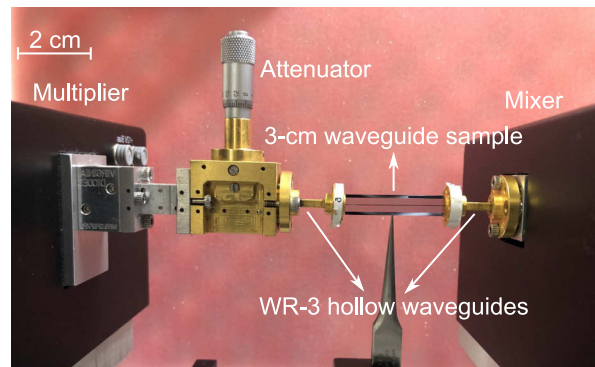
waveguide ports. Thus, to enable efficient transition, the tapered structures are inserted into the rectangular waveguides, so that the modes can couple between the hollow waveguides and the sample. In this way, a dielectric waveguide sample positioned between the transmitter and the receiver can be measured with minimal coupling losses.

The transmission coefficients $|S_{21}|$ of the fabricated waveguides displayed in Fig. 4 for both polarizations are measured with the waveguide length varying from 1 to 3 cm as shown in Fig. 6. The measurement setup has been discussed in the method section. The measurements agree well with the simulations in terms of the transmission levels. From the results shown in Fig. 6(c)–6(d), the measured transmission for the E_{11}^x mode for each length varies from -2.5 to -0.1 dB over 260 to 390 GHz and from -2 to -0.05 dB for the E_{11}^y mode over the band. Both the simulated and measured transmission levels are lower at the lower frequencies because of the higher coupling losses caused by the slight impedance and mode mismatches between the sample and the feed. Due to the evanescent fields of the dielectric waveguide, the transmission measurements are highly sensitive to the alignment with respect to the feeding hollow waveguides. Despite the aid of micromechanical positioners in the alignment, the measured transmission profiles exhibit larger fluctuations than that of simulations. In view of this fact, we conclude that the attenuation of the waveguide is too small to be extracted directly, but can be approximated by comparing and averaging the losses of waveguides with multiple lengths. As shown in Fig. 6(e), the simulated attenuation coefficient varies from 0.003 to 0.055 dB/cm for the E_{11}^x mode, while it ranges from 0.003 to 0.048 dB/cm for the E_{11}^y mode over 260 to 400 GHz. However, the measured attenuation coefficient varies from 0.01 to 0.09 dB/cm for the E_{11}^x mode, and from 0.01 to 0.07 dB/cm for the E_{11}^y mode over 260 to 380 GHz with an average value of around 0.05 dB/cm.

This level of loss for the proposed effective-medium-cladded waveguides is comparable to the extremely low-loss photonic crystal waveguides [15,17] and bare high-resistivity dielectric waveguides [24], which exhibited less than 0.1 dB/cm attenuation over their operation band. However, the loss of the proposed waveguides is more than one order of magnitude lower than a



(a)



(b)

Fig. 5. Transmission measurement setup. (a) Block diagram, and (b) actual setup. SG: signal generator, SA: signal analyser, THz: terahertz frequency, LO: local oscillator, IF: intermediate frequency.

commercial WR-2.8 rectangular waveguide (0.287 – 0.436 dB/cm) [37]. In addition, the radiation loss caused by a 90° bending with a radius of 2 mm is simulated in CST Microwave Studio. An average bending loss of less than 0.1 dB per bending for the two modes is achieved over 310–400 GHz and it is comparable to that of the photonic crystal waveguide [15] with a bending loss of about 0.2 dB per bending around 323–331 GHz. However, at the lower frequencies from 260 to 310 GHz, the bending loss varies from 5.5 to 0.5 dB per bending for the E_{11}^x mode and from 3.1 to 0.1 dB per bending for the E_{11}^y mode. The higher bending losses can be compensated by increasing the bending radius at the expense of structural compactness. A comparison between the proposed dielectric interconnect and other guiding structures based on microwave and photonics technologies is shown in Table 1. The comparison demonstrates that at terahertz frequencies the proposed waveguides exhibit broad bandwidth, low loss, and low dispersion, while supporting two orthogonal fundamental modes.

3.2. Communications measurements

To validate the waveguide performance in terahertz communications, bit-error-rate testing experiments are performed and an uncompressed 4K-resolution video transmission is demonstrated. A diagram of the measurement system is shown in Fig. 7. On the transmitter side, two tunable near-infrared laser sources generate a beat optical signal that is modulated with the signal from a pulse-pattern generator or a 4K-resolution video player. Amplified by the EDFA, the modulated signal is down-converted to the terahertz signal by a UTC-PD and then coupled to the dielectric waveguide through a WR-3 hollow waveguide. On the receiver side, a SBD is used to retrieve the modulating data from the received terahertz signal. The data signal is then reshaped by a preamplifier and a limiting amplifier. The data quality is then measured by a bit-error rate tester

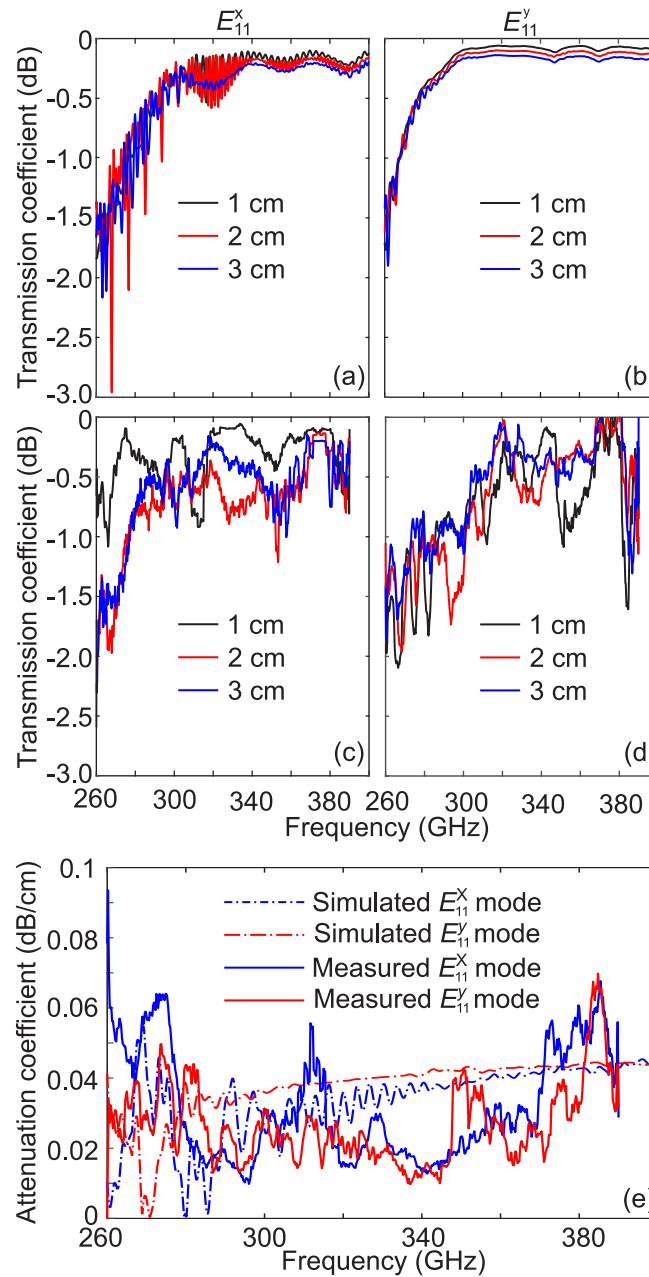


Fig. 6. Transmission and attenuation coefficients of the waveguides. (a, b) Simulated, (c, d) measured transmission coefficients, and (e) simulated and measured attenuation coefficients extracted from (a–d). The E_{11}^x and E_{11}^y modes are represented in (a, c) and (b, d), respectively. A realistic loss tangent of 3×10^{-5} for the silicon is used in full-wave simulation by CST Microwave Studio.

Table 1. Comparison of interconnects at terahertz and millimetre-wave frequencies.

	Frequency (GHz)	Bandwidth ^a	Losses (dB/cm)	Dispersions	Modes	Integrability
Microwave-based						
Coplanar waveguide [18]	200–400 ^b	–	5–22	Low	Quasi-TEM	Yes
Metallic microstrip line [20]	220–330 ^b	–	3.7–5.0	Low	Quasi-TEM	Yes
Hollow waveguide [37]	260–400	42.4%	0.287–0.436	High	TE ₁₀	No
SIIG waveguide [11]	83–99	17.6%	0.45	Low	E_{11}^y	Yes
SIIG waveguide [12]	110–170	42.9%	0.35	Low	E_{11}^y	Yes
Photonics-based						
Dielectric microstrip line [14]	750–925	20.9%	0.23–1.2	Low	E_{11}^y	Yes
SOI waveguide [13]	500–580	14.8%	0.46	Low	E_{11}^x	Yes
PC waveguide [17]	324–361	10.8%	< 0.1	High	TE	Yes
Ribbon waveguide [24]	140–220	44.4%	0.087	Low	E_{11}^x and E_{11}^y	No
This work	260–400	42.4%	0.05	Low	E_{11}^x and E_{11}^y	Yes

^aThe bandwidth is for dominant modes.

^bThe frequency range is limited by the bandwidth of measurement system.

and an oscilloscope, while for the uncompressed 4K-resolution video transmission measurement, the signal can be displayed on a 4K television after a digital signal converter.

A bit-error-rate test is conducted with a 3-cm waveguide sample for the E_{11}^x mode over 300 to 385 GHz. As shown in Fig. 8(a), the error-free data rate is reasonably stable over a relatively wide bandwidth (310–370 GHz), which is attributed to the extremely low loss and low dispersion of the waveguide. At 335 GHz, the maximum measured data rate of 28 Gbit/s is achieved corresponding to the highest 3-dB bandwidth shown in Fig. 3(c). The measurable maximum data rates are limited by the bandwidths of various components in the measurement setup. Specifically,

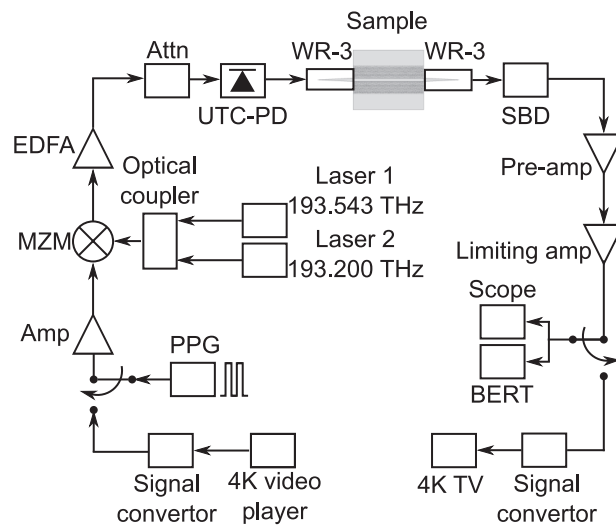


Fig. 7. Communication measurement diagram. PPG: pulse-pattern generator, Amp: amplifier, MZM: Mach-Zehnder modulator, EDFA: erbium-doped fibre amplifier, Attn: attenuator, UTC-PD: uni-travelling carrier photodiode, WR-3: WR-3 hollow waveguide, SBD: Schottky barrier diode, Scope: oscilloscope, and BERT: bit-error-rate tester.

the degradations of the data rate at lower and higher frequencies are due to the roll-off effects of the uni-travelling carrier photodiode (UTC-PD) and Schottky barrier diode (SBD). Meanwhile, the eye-diagrams have clear opening as shown in Figs. 8(b)–8(d) for 330, 335 and 385 GHz. An uncompressed 4K-resolution video transmission is performed as shown in Fig. 8(e), and the demonstration can be found in [Visualization 1](#). It demonstrates that the proposed waveguide can support a real-time uncompressed 4K video data transmission at the speed of 6 Gbit/s. The 3-cm sample in this study is mainly for a proof of the concept, and this type of waveguide is not intended for long-range transmission. The proposed interconnects are rather for a terahertz integrated platform or frontend to accommodate various passive and active components for different terahertz applications. For example, such a frontend can be used to interface with wireless and fiber links similar to the photonic crystal waveguide in [38].

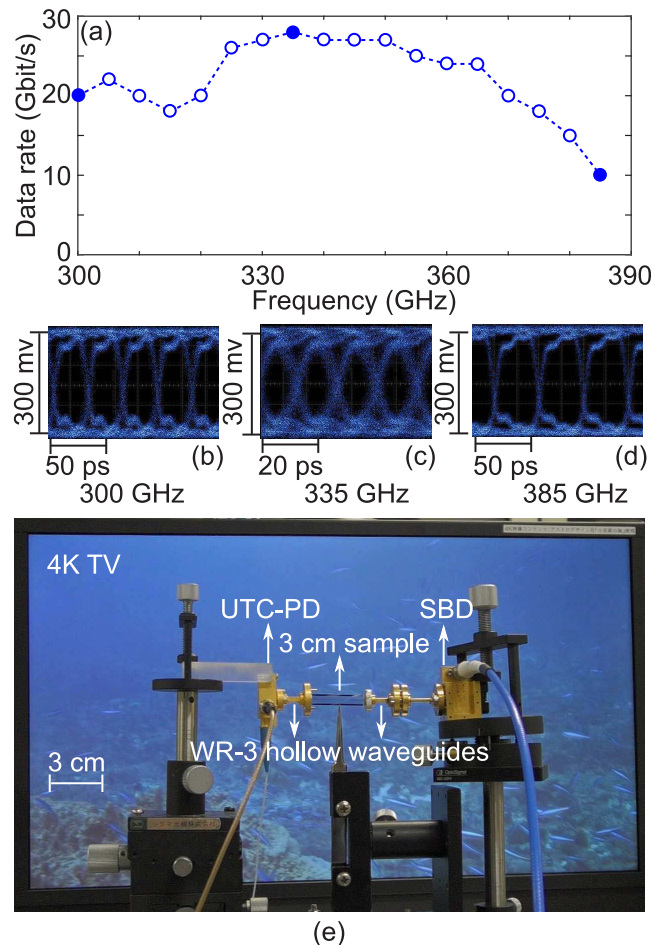


Fig. 8. Communications measurement results. (a) Measured error-free data rate as a function of frequency over 300 to 385 GHz. The results are discrete and the lines are for visual guidance. Eye diagrams at the carrier frequencies of (b) 300 GHz (20 Gbit/s), (c) 335 GHz (28 Gbit/s), and (d) 385 GHz (10 Gbit/s). (e) Uncompressed 4K-resolution video transmission demonstration (See Visualization).

4. Conclusion

A design of low-loss, low dispersion dielectric waveguides based on effective medium claddings has been proposed. The waveguides are created from a single silicon wafer and do not include other materials. The effective medium claddings enable a self-supporting and integrated platform while yielding a totally different guiding mechanism compared with photonic bandgap claddings. The designed waveguides can support single dominant E_{11}^x and E_{11}^y modes over 260 to 400 GHz, which is equivalent to a relative bandwidth of 42.4%. An average measured attenuation coefficient of around 0.05 dB/cm is achieved for both E_{11}^x and E_{11}^y modes over the operation frequency range. To characterize the transmission and communications performance, waveguide samples with various lengths have been fabricated. The measurement shows a system-limited maximum error-free data rate of 28 Gbit/s at 335 GHz. Importantly, the proposed waveguide delivers much needed bandwidth, dispersion, and mode orthogonality that are not available from photonic crystal waveguides. With demonstrated performance and form-factor, the proposed waveguide concept can be used as a platform to accommodate various passive/active devices in future terahertz more general systems [9,27,28]. The concept of the waveguide is applicable to operation at infrared and optical frequencies.

Funding

Japan Science and Technology Agency (#JPMJCR1534); Australian Research Council (ARC DP170101922, ARC DP180103561).

Acknowledgments

The authors would like to thank Dr. Frank Demming-Jassen for his technical support in CST simulations. The Quadro P6000 GPU used for this research was donated by NVIDIA Corporation to the Terahertz Engineering Laboratory, The University of Adelaide.

Disclosures

The authors declare no competing financial interests. Readers are welcome to comment on the online version of the manuscript. Correspondence and requests for materials should be addressed to Withawat Withayachumnankul (withawat@adelaide.edu.au) and Masayuki Fujita (fujita@ee.es.osaka-u.ac.jp).

References

1. Cisco, *Cisco Visual Networking Index: Forecast and Methodology, 2016-2021* (Cisco, 2017).
2. T. Nagatsuma, G. Ducournau, and C. C. Renaud, "Advances in terahertz communications accelerated by photonics," *Nat. Photonics* **10**(6), 371–379 (2016).
3. A. Goldsmith, *Wireless Communications* (Cambridge University, 2005).
4. J. Ma, R. Shrestha, L. Moeller, and D. M. Mittleman, "Invited article: Channel performance for indoor and outdoor terahertz wireless links," *APL Photonics* **3**(5), 051601 (2018).
5. S. Koenig, D. Lopez-Diaz, J. Antes, F. Boes, R. Henneberger, A. Leuther, A. Tessmann, R. Schmogrow, D. Hillerkuss, and R. Palmer, "Wireless sub-thz communication system with high data rate," *Nat. Photonics* **7**(12), 977–981 (2013).
6. K. Sengupta, T. Nagatsuma, and D. M. Mittleman, "Terahertz integrated electronic and hybrid electronic–photonic systems," *Nat. Electron.* **1**(12), 622–635 (2018).
7. G. Gallot, S. Jamison, R. McGowan, and D. Grischkowsky, "Terahertz waveguides," *J. Opt. Soc. Am. B* **17**(5), 851–863 (2000).
8. R. McGowan, G. Gallot, and D. Grischkowsky, "Propagation of ultrawideband short pulses of terahertz radiation through submillimeter-diameter circular waveguides," *Opt. Lett.* **24**(20), 1431–1433 (1999).
9. W. Withayachumnankul, M. Fujita, and T. Nagatsuma, "Integrated silicon photonic crystals toward terahertz communications," *Adv. Opt. Mater.* **6**(16), 1800401 (2018).
10. N. Dolatsha, "Hybrid integrated of millimeter wave circuits based on low-loss dielectric waveguides," Ph.D. thesis, ETH Zurich (2013).
11. A. Patrovsky and K. Wu, "Substrate integrated image guide (SIIG)- A planar dielectric waveguide technology for millimeter-wave applications," *IEEE Trans. Microwave Theory Tech.* **54**(6), 2872–2879 (2006).

12. A. Taeb, L. Chen, S. Gigoyan, M. Basha, G. Rafi, S. Chaudhuri, and S. Safavi-naeini, "A silicon image guide (SIG) technology platform for high performance sub-millimeter-wave passive structures," in *IEEE MTT-S International Microwave Symposium (IMS)*, (IEEE, 2016), pp. 1–4.
13. H. Amarloo, N. Ranjkesh, and S. A. Safavi-Naeini, "Terahertz silicon-BCB-quartz dielectric waveguide: an efficient platform for compact THz systems," *IEEE Trans. Terahertz Sci. Technol.* **8**(2), 201–208 (2018).
14. H. Zhu, Q. Xue, J. Hui, and S. W. Pang, "Design, fabrication, and measurement of the low-loss SOI-based dielectric microstrip line and its components," *IEEE Trans. Terahertz Sci. Technol.* **6**, 696–705 (2016).
15. K. Tsuruda, M. Fujita, and T. Nagatsuma, "Extremely low-loss terahertz waveguide based on silicon photonic-crystal slab," *Opt. Express* **23**(25), 31977–31990 (2015).
16. M. Fujita and T. Nagatsuma, "Photonic crystal technology for terahertz system integration," in *Terahertz Physics, Devices, and Systems X: Advanced Applications in Industry and Defense*, vol. 9856 (International Society for Optics and Photonics, 2016), p.98560P.
17. X. Yu, M. Sugeta, Y. Yamagami, M. Fujita, and T. Nagatsuma, "Simultaneous low-loss and low-dispersion in a photonic-crystal waveguide for terahertz communications," *Appl. Phys. Express* **12**(1), 012005 (2019).
18. M. Y. Frankel, S. Gupta, J. A. Valdmanis, and G. A. Mourou, "Terahertz attenuation and dispersion characteristics of coplanar transmission lines," *IEEE Trans. Microwave Theory Tech.* **39**(6), 910–916 (1991).
19. J. Zhang and T. Y. Hsiang, "Dispersion characteristics of coplanar waveguides at subterahertz frequencies," *J. Electromagn. Waves Appl.* **20**(10), 1411–1417 (2006).
20. K. Murano, I. Watanabe, A. Kasamatsu, S. Suzuki, M. Asada, W. Withayachumnankul, T. Tanaka, and Y. Monnai, "Low-profile terahertz radar based on broadband leaky-wave beam steering," *IEEE Trans. Terahertz Sci. Technol.* **7**(1), 60–69 (2016).
21. K. Wu, D. Deslandes, and Y. Cassivi, "The substrate integrated circuits-a new concept for high-frequency electronics and optoelectronics," in *6th International Conference on Telecommunications in Modern Satellite, Cable and Broadcasting Service, 2003. TELSIKS 2003.*, vol. 1 (IEEE, 2003), pp. P–III.
22. M. Belt, M. L. Davenport, J. E. Bowers, and D. J. Blumenthal, "Ultra-low-loss Ta₂O₅-core/SiO₂-clad planar waveguides on Si substrates," *Optica* **4**(5), 532–536 (2017).
23. S. A. Miller, M. Yu, X. Ji, A. G. Griffith, J. Cardenas, A. L. Gaeta, and M. Lipson, "Low-loss silicon platform for broadband mid-infrared photonics," *Optica* **4**(7), 707–712 (2017).
24. A. Malekabadi, S. A. Charlebois, D. Deslandes, and F. Boone, "High-resistivity silicon dielectric ribbon waveguide for single-mode low-loss propagation at F/G-bands," *IEEE Trans. Terahertz Sci. Technol.* **4**(4), 447–453 (2014).
25. K. K. Lee, D. R. Lim, L. C. Kimerling, J. Shin, and F. Cerrina, "Fabrication of ultralow-loss Si/SiO₂ waveguides by roughness reduction," *Opt. Lett.* **26**(23), 1888–1890 (2001).
26. J. Dai, J. Zhang, W. Zhang, and D. Grischkowsky, "Terahertz time-domain spectroscopy characterization of the far-infrared absorption and index of refraction of high-resistivity, float-zone silicon," *J. Opt. Soc. Am. B* **21**(7), 1379–1386 (2004).
27. X. Yu, Y. Hosoda, T. Miyamoto, K. Obata, J.-Y. Kim, M. Fujita, and T. Nagatsuma, "Terahertz fibre transmission link using resonant tunnelling diodes integrated with photonic-crystal waveguides," *Electron. Lett.* **55**(7), 398–400 (2019).
28. X. Yu, J.-Y. Kim, M. Fujita, and T. Nagatsuma, "Efficient mode converter to deep-subwavelength region with photonic-crystal waveguide platform for terahertz applications," *Opt. Express* **27**(20), 28707–28721 (2019).
29. P. Cheben, R. Halir, J. H. Schmid, H. A. Atwater, and D. R. Smith, "Subwavelength integrated photonics," *Nature* **560**(7720), 565–572 (2018).
30. H. Mosallaei and Y. Rahmat-Samii, "Photonic band-gap (PBG) versus effective refractive index: a case study of dielectric nanocavities," in *IEEE Antennas and Propagation Society International Symposium.*, (IEEE, 2000), pp. 338–341.
31. J. Birman, S. F. Edwards, R. Friend, M. Rees, D. Sherrington, and G. Veneziano, *Effective Medium Theory Principles and Applications* (Oxford Science Publications, 2009), II ed.
32. A. V. Subashiev and S. Luryi, "Modal control in semiconductor optical waveguides with uniaxially patterned layers," *J. Lightwave Technol.* **24**(3), 1513–1522 (2006).
33. E. A. J. Marcatili, "Dielectric rectangular waveguide and directional coupler for integrated optics," *Bell Syst. Tech. J.* **48**(7), 2071–2102 (1969).
34. K. Okamoto, *Fundamentals of Optical Waveguides* (Academic, 2007), II ed.
35. L. Chrostowski and M. Hochberg, *Silicon Photonics Design: from Devices to Systems* (Cambridge University, 2015).
36. G. P. Agrawal, *Fiber-Optic Communication Systems* (John Wiley & Sons, 2012).
37. Virginia Diodes Inc., *Waveguide Band Designations* (Diodes Inc, 2010).
38. X. Yu, T. Miyamoto, K. Obata, Y. Hosoda, J.-Y. Kim, M. Fujita, and T. Nagatsuma, "Direct terahertz communications with wireless and fiber links," in *2019 44th International Conference on Infrared, Millimeter, and Terahertz Waves (IRMMW-THz)*, (IEEE, 2019), pp. 1–2.